

1 Structural and electronic properties of Cu_4O_3
2 (paramelaconite): the role of native impurities

3 Aleksandar Živković^{1,2}, Jacobina Sheehama³, Michael E. A. Warwick⁴,
4 Daniel R. Jones⁴, Claire Mitchel¹, Daniel Likius³, Veikko Uahengo³,
5 Nelson Y. Dzade¹, Sankar Meenakshisundaram¹, Charles W. Dunnill^{4,*},
6 and Nora H. de Leeuw^{1,2,5,*}

7 ¹*Cardiff University, School of Chemistry, Main Building Park Place, Cardiff CF10 3AT, United*
8 *Kingdom*

9 ²*Department of Earth Sciences, Utrecht University, Princetonlaan 8a, 3548CB Utrecht, The*
10 *Netherlands*

11 ³*Department of Chemistry and Biochemistry, University of Namibia, 340 Mandume Ndemufayo*
12 *Avenue, Windhoek 9000, Namibia*

13 ⁴*Energy Safety Research Institute, Swansea University, Bay Campus, Fabian Way, SA1 8EN United*
14 *Kingdom*

15 ⁵*School of Chemistry, University of Leeds, Woodhouse Lane, Leeds LS2 9JT, United Kingdom*

16 * *Corresponding authors: C.Dunnill@swansea.ac.uk, N.H.deLeeuw@leeds.ac.uk*

17 **Abstract**

18 Hybrid density functional theory has been used to study the phase stability and
19 formation of native point defects in Cu_4O_3 . This intermediate copper oxide com-
20 pound, also known as paramelaconite, was observed to be difficult to synthesize due
21 to stabilization issues between mixed-valence Cu^{1+} and Cu^{2+} ions. The stability
22 range of Cu_4O_3 was investigated and shown to be realized in an extremely narrow
23 region of phase space, with Cu_2O and CuO forming readily as competing impu-
24 rity phases. The origin of p -type conductivity is confirmed to arise from specific
25 intrinsic copper vacancies occurring on the 1+ site. Away from the outlined stabil-
26 ity region, the dominant charge carriers become oxygen interstitials, impairing the
27 conductivity by creating deep acceptor states in the electronic band gap region and
28 driving the formation of alternative phases. This study further demonstrates the
29 inadequacy of native defects as a source of n -type conductivity and complements
30 existing experimental findings.

1 Introduction

Paramelaconite (Cu_4O_3) is the least explored oxide of copper. First reports on the structure of Cu_4O_3 date back to the works of Clifford Frondel [1] and Datta *et al* [2], who defined paramelaconite as an oxygen-deficient tetragonal copper oxide, where the omission of oxygen atoms is compensated by the appearance of cuprous ions in place of cupric ones. However, both proposed structures had a unit cell content of $\text{Cu}_{16}\text{O}_{14}$, which was later attributed to the presence of admixed CuO in the sample. A refined structure with the unit cell content of $\text{Cu}_{16}\text{O}_{12}$ (i.e., Cu_4O_3) was identified by O’Keeffe and Bovin [3]. The correct chemical formula of paramelaconite is $\text{Cu}_2^+\text{Cu}_2^+\text{O}_3$, with two distinct copper atoms, $\text{Cu}(1)$ and $\text{Cu}(2)$. The first one, $\text{Cu}(1)$, is cuprous copper and has two nearest neighbour oxygen atoms, $\text{O}(1)$, forming collinear bonds of length 1.87 Å as found in Cu_2O . In contrast, $\text{Cu}(2)$ is cupric copper and is surrounded by four oxygen atoms in an almost square planar configuration with bond lengths varying between 1.92 Å and 1.97 Å. Paramelaconite was indexed with a tetragonal cell with lattice parameters reading $a = b = 5.837$ Å and $c = 9.932$ Å (space group $I4_1/amd$, Number 141). The non-equivalent atomic positions are listed in Table 1.

Structural stability. The structure of Cu_4O_3 can be thought of as derived from CuO by ordered removal of oxygen atoms or derived from Cu_2O by ordered insertion of oxygen atoms – an intermediate stoichiometry between cupric and cuprous oxide. The name paramelaconite itself was derived from an old term used to describe the mineral CuO , namely melaconite [4]. Due to its unique stoichiometry, it is very difficult to synthesize Cu_4O_3 and particularly stabilize the mixed Cu^{1+} and Cu^{2+} valence ions [5]. The first experimental observation and successful synthesis of Cu_4O_3 dates back to the work of Long *et al* [6]. They observed that the reduction of CuO to Cu using high resolution electron microscopy proceeded via at least two intermediate phases – Cu_4O_3 and Cu_2O . Paramelaconite was observed to be sensitive to air oxidation due to different valence copper atoms within the structure, hence the observed decomposition into Cu_2O and Cu at 350° C and pure Cu at 500° C. However, it was observed to be stable in air at 250° C for 0.55 μm thick samples and 350° C for 3.2 μm thick films [7]. In other words, the thickness and orientation of the films influence the stability and conversion temperature of Cu_4O_3 in air. In a separate study, Cu_4O_3 was observed to be stable up to 250° C (520 K) when annealed in air [8]. It was also emphasized that upon annealing of Cu_4O_3 at 410° C (683 K) a phase conversion into CuO is observed, as well as a further conversion into Cu_2O at 450° C (723 K). Similarly, experiments conducted by Wang *et al* [9] observed a decomposition of candy-like Cu_4O_3 micro-structures into CuO and Cu_2O at 400° C (673 K). More recently, a copper-oxide based catalyst powder enriched with paramelaconite was found to be stable and perform well under industrially relevant current densities, forming ethylene as the main product [10]. Patwary *et al* synthesized Cu_4O_3 films in an ambient

Table 1: Wyckoff sites and fractional coordinates of non-equivalent atomic positions in Cu_4O_3 after O’Keeffe and Bovin [3].

Atom	Site Symmetry	x	y	z
Cu^{1+}	8d	0.00000	0.00000	0.50000
Cu^{2+}	8c	0.00000	0.00000	0.00000
O-1	8e	0.00000	0.25000	0.61730
O-2	4a	0.00000	0.75000	0.12500

of Ar and O_2 plasma using a pure Cu target and identified that oxygen partial pressures of 7.9% – 9.1% were required to grow pure phase Cu_4O_3 [11].

Electronic properties. Based on UV-visible transmission measurements, a direct gap of 2.47 eV and an indirect band gap of 1.34 eV were measured [7] (see Table 2 for complete results). The measured absorption coefficient for Cu_4O_3 reaches a value of $1 \cdot 10^5 \text{ cm}^{-1}$ at a value of 2.4 eV. The rise of absorbance ($\lambda \leq 500 \text{ nm}$) was derived from the direct band gap of 2.25 eV, while the light absorption corresponding to the indirect band gap (1.5 eV) was found to be relatively less effective [12].

Magnetic and transport properties. Paramelaconite was measured to order antiferromagnetically below 40 K with a propagation vector $\vec{k} = (\frac{1}{2}, \frac{1}{2}, \frac{1}{2})$ with respect to the reciprocal basis of the conventional body centred cell [13]. The authors were unable to explain the observed magnetic ordering within models limited to isotropic super-exchange interactions, speculating upon the need to invoke higher order interactions or anisotropic exchange. Djurek *et al* [14] observed an antiferromagnetic ordering of nanoscaled Cu_4O_3 at $T < 55 \text{ K}$ together with an additional transition at $T = 120 \text{ K}$, whose ordering was not clarified. Hall effect measurements indicate that Cu_4O_3 is a *p*-type semiconductor [8]. The reported activation energy, in other words the thermal energy required for holes to jump into the valence band, is read as 0.14 eV, which lies around the reported values of CuO (0.12 – 0.16 eV) but below those of Cu_2O (0.20 – 0.24 eV). Thermo-power measurements confirmed the *p*-type conductivity of Cu_4O_3 samples with a single thermal hole activation energy (ionization energy of acceptors) of 0.12 eV [11]. Two high temperature conduction activation energies were measured at 0.29 eV and 0.41 eV (depending on oxygen flow rate synthesis conditions) and one low temperature conduction activation energy of $\approx 0.21 \text{ eV}$.

Theoretical investigations. Initial theoretical studies of Cu_4O_3 date back, to the best knowledge of the author, to a hybrid-DFT (B3LYP) study of Tejada-Rosales *et al* [15]. Within their work, they investigated the structure and magnetic exchange interactions (between nearest neighbouring Cu atoms) and obtained values of $J_a = -11.1 \text{ cm}^{-1}$ (for the interaction along of Cu atoms along the chains) and $J_c = -9.8 \text{ cm}^{-1}$ (for the interaction between neighbouring perpendicular chains). More recently, DFT calculations using

Table 2: Electronic properties of Cu_4O_3 found in existing literature.

Electronic band gap (indirect)	1.34 eV [7], 1.5 eV [19]
Electronic band gap (direct)	2.47 eV [7], 1.75 eV [20]
	2.3 eV [19]

the L(S)DA+ U approach were used to study the vibrational properties of both CuO and Cu_4O_3 , obtaining good agreement with experimental values [16]. A clear distinction between CuO and Cu_4O_3 was observed based on the peak positions in the Raman spectrum, making it a useful probe for phase analysis.

Heinemann *et al* [17] studied the structural stability and electronic structure of all three copper oxides using the LDA+ U and hybrid (HSE06) functional calculations within DFT. The reported electronic energy gaps are in good agreement with experiment for Cu_2O , while CuO and Cu_4O_3 showed discrepancies between theory and experiment.

Debbichi *et al* [18] studied the lattice dynamics for paramelaconite using the LDA+ U approximation. From the calculated phonon band structures a dynamic stability was noted, as no soft modes were detected. Furthermore, the magnetic exchange coupling constants between neighbouring Cu^{2+} sites were calculated, yielding values of $J_1 = -18.2$ meV and $J_2 = -12.6$ meV, implying frustrated antiferromagnetism within Cu_4O_3 . By including vibrational energy contributions to the total energy, the influence on the instability of Cu_4O_3 at elevated temperatures was illustrated.

Recently, Wang *et al* [21] performed calculations within the GW method (highly accurate many-body perturbation technique) of the full optical absorption spectrum (both in the independent particle approximation and including excitonic effects) and quasi-particle densities of state for all three copper oxides. The GW calculations predict an indirect gap of 0.84 eV and a direct gap of 1.59 eV with an absorption onset of 1.61 eV in the IPA for Cu_4O_3 . Excitonic effects were found to cause a redshift in the absorption spectrum of about 150 meV. Despite the different subgap absorption mechanisms proposed, the prediction of an indirect band gap for Cu_4O_3 was confirmed through the experimentally and theoretically measured absorption spectrum.

Aim of current study. The majority of works concerning Cu_4O_3 treat the determination of its structural parameters and composition (experimentally), or electronic structure and absorption spectra (theoretically). However, little is known about defects present in Cu_4O_3 , apart from its p -type conductivity, stemming from Hall measurement. The question of creating n -type Cu_4O_3 was neglected as well. The current work presents a joint experimental and theoretical study of the electronic ground state properties of Cu_4O_3 . In addition, native impurities occurring in Cu_4O_3 are explored (using hybrid-DFT) together with the single-particle levels they eventually form in the pristine electronic band structure. An attempt is made to answer the following questions: (i) What is the role of simple impurities in the stability of Cu_4O_3 ? (ii) Can Cu_4O_3 be created intrinsically

133 *n*-type? In order to do so, a comprehensive first-principles study of the geometry and
134 electronic structure of Cu₄O₃ with induced defects was undertaken.

135 2 Experimental and Computational details

136 2.1 Experiments

137 **Materials** All reagents were of analytical grade and used without further purifica-
138 tion. Distilled water was used in all experiments. The powders were synthesized using a
139 solvothermal method adapted from Zhao *et al* [5]. In a synthesis, N,N-dimethylformamide
140 (DMF) and ethanol were mixed in a 1:2 volume ratio to form the reaction solvent.
141 Cu(NO₃)₂·3H₂O was dissolved in 75.0 mL of this solvent to form a precursor solution
142 of 0.07 M. The precursor solution was stirred for 15 minutes to form a clear solution.
143 The reactions took place in a 150 mL white Teflon lined steel autoclave as well as in a
144 hydrothermal bomb. In an autoclave attempt: The autoclave was sealed and maintained
145 at 130° C for 9 hours. In a hydrothermal bomb attempt: the reaction took place in a
146 150 mL white Teflon liner which was placed into the hydrothermal bomb and heated in an
147 oven at 130° C for 9 hours. In both reactions, the reaction was cooled down naturally to
148 room temperature. The products were collected by centrifugation and washed with water
149 and ethanol several times, before dried at 40° C in an oven. The samples synthesized in
150 the autoclave and hydrothermal bomb were named A2 and A3, respectively.

151 **Characterization** The crystal structures of A2 and A3 were studied by X-ray diffrac-
152 tion (XRD) using a Bruker D8 Advance X-ray diffractometer. Diffractograms were mea-
153 sured using a Cu-K α radiation source (1.5418 Å) in the range of 10.0° – 80.0°. Molec-
154 ular analysis of the samples was performed by Fourier transform Infrared (FT-IR) spec-
155 troscopy using IR Thermo Scientific Smart iTR spectrophotometer. The spectropho-
156 tometer recorded in the wavenumber range of 4000 cm⁻¹ to 400 cm⁻¹. UV-Vis diffuse
157 reflectance spectroscopy (DRS) was used to study the optical properties of A2 and A3,
158 using an Agilent Cary UV-Vis spectrophotometer. The spectra were recorded in the
159 range of 400 nm – 800 nm.

160 2.2 Calculations

161 Results computed and presented in this work were based on spin polarized DFT-based
162 calculations performed with the Vienna Ab-initio Simulation Package [22]. The interac-
163 tions between core and valence electrons were represented using the projector augmented
164 wave (PAW) method [23]. The general gradient approximation (GGA) [24] exchange-
165 correlation (XC) functional with the Perdew–Burke–Ernzerhof (PBE) parametrization

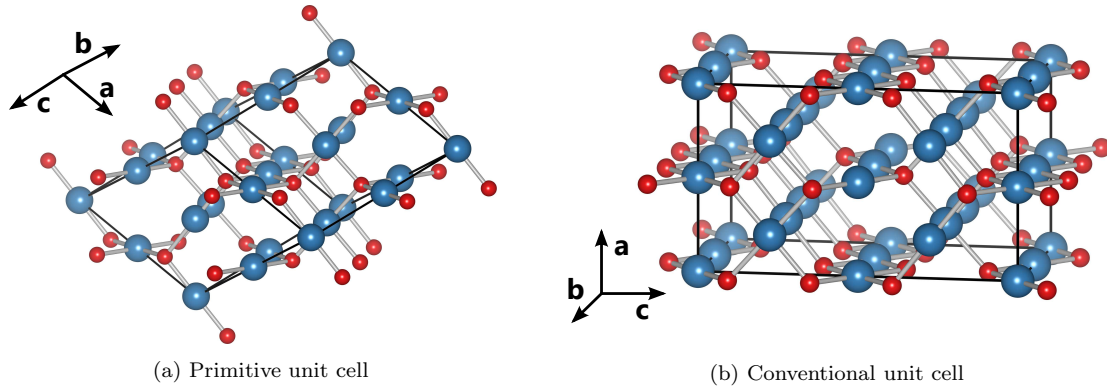


Figure 1: Schematic representation of different ways to define the modelling unit cell of Cu_4O_3 . Blue and red sphere represent copper and oxygen atoms, respectively.

166 was employed for DFT+ U within the formalism of Dudarev *et al* [25], with an $U_{\text{eff}} = 8\text{eV}$
 167 identified in an earlier study [26]. For the hybrid-DFT calculations, the HSE06 XC func-
 168 tional was used [27, 28, 29], with a screening parameter of 0.2\AA^{-1} . Long distance disper-
 169 sion corrections were included using the D3 approach of Grimme *et al* [30]. The plane
 170 wave expansion cutoff was set to 500 eV and the force convergence criterion to cell relax-
 171 ation was 0.01 eV/\AA . Monkhorst-Pack [31] meshes ($5 \times 5 \times 5$ for the primitive unit cell,
 172 $5 \times 5 \times 3$ for conventional unit cell, and single Γ point for the $2 \times 2 \times 2$ supercell) were em-
 173 ployed to sample the Brillouin zone in reciprocal space. Band structure calculations were
 174 performed at the optimized structure along high-symmetry directions obtained from the
 175 Bilbao Crystallographic Server [32, 33, 34] and plotted using the Wannier90 code [35, 36].
 176 The phase stability diagram of Cu_4O_3 for a range of accessible chemical potentials was
 177 computed using the CPLAP (Chemical Potential Limits Analysis Program)[37], taking
 178 into account its limiting competing phases. The extent of defect charge distribution was
 179 studied using the Bader scheme as implemented in the Henkelman code [38, 39, 40].
 180 Graphical drawings were produced using VESTA [41]. Excitonic and spin-orbit coupling
 181 effects were not taken into account.

182 B3LYP calculations were first performed using the all-electron CRYSTAL17 code
 183 [42, 43], in conjunction with triple- ζ -valence + polarization Gaussian-type basis sets op-
 184 timized for copper oxides by Linnera *et al* [44, 45]. In CRYSTAL, the convergence of the
 185 real-space summation of the Coulomb and exchange contributions to the Hamiltonian
 186 matrix is controlled by five overlap criteria. The values used in this study were 10^{-7} ,
 187 10^{-7} , 10^{-7} , 10^{-7} , and 10^{-14} . A Monkhorst-Pack shrinking factor of 8 was used to sample
 188 the first Brillouin zone and a denser Gilat net consisting of 16 points was used in the
 189 evaluation of the Fermi energy and density matrix [42]. The tuning of the exact exchange
 190 fraction used in B3LYP was done according to the self-consistent scheme proposed by
 191 Skone *et al* [46] and implemented by Erba *et al* [47]. Following that procedure, the system-
 192 specific exact exchange fraction, defined as inversely proportional to the static electronic
 193 dielectric constant ϵ_{∞} , is calculated iteratively until it changes by less than 0.1% be-

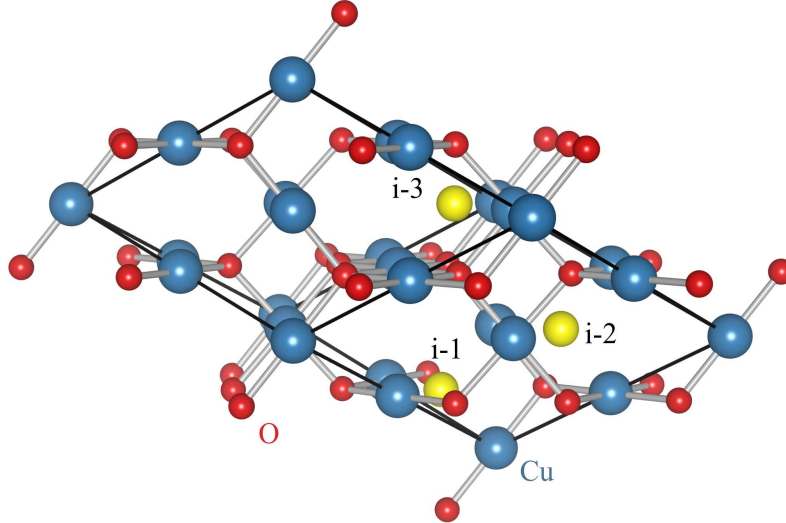


Figure 2: Schematic representation of identified suitable interstitial position within the primitive crystal lattice of Cu_4O_3 . Interstitial positions are labelled with black letters from i-1 to i-3.

194 tween two subsequent iterations. CRYSTAL17 uses a fully-automated, computationally-
 195 efficient implementation of the self-consistent (global) hybrid functional, where the di-
 196 electric functional is computed adopting a Coupled-Perturbed-Hartree-Fock/Kohn-Sham
 197 (CPHF/KS) approach [42]. A value of 0.17407 (17.407 % of exact exchange) used within
 198 B3LYP was obtained and demonstrated to yield accurate results for Cu_4O_3 [48].

199 Similarly to CuO , the conventional and primitive unit cells of Cu_4O_3 (illustrated in
 200 Figure 1) exhibit different geometries. In order to transform from the primitive to the
 201 conventional modelling cell, the following transformations were applied:

$$\begin{array}{c}
 P \rightarrow C \\
 \left(\begin{array}{ccc}
 -\frac{1}{2} & \frac{1}{2} & \frac{1}{2} \\
 \frac{1}{2} & -\frac{1}{2} & \frac{1}{2} \\
 \frac{1}{2} & \frac{1}{2} & -\frac{1}{2}
 \end{array} \right) \quad (1)
 \end{array}$$

202 where P and C stand for primitive and conventional, respectively. The simulation cell,
 203 in both the primitive and conventional crystallographic cell case was carefully tested and
 204 set up in such a way to reproduce the appropriate magnetic propagation vector discussed
 205 earlier. The equivalence between the two modelling cells was confirmed and the primitive
 206 one chosen for the subsequent defects study, in order to reduce the computational cost
 207 when compared to the conventional cell.

208 **Modelling of defects** Studied native defects in Cu_4O_3 include simple vacancies (V_{Cu}
 209 and V_{O}), antisites (Cu_{O} and O_{Cu}), and interstitials in three different positions within the

simulation cell (Cu_{i-n} and O_{i-n} , with $n = 1, 2, 3$, identified using the PyCDT package [49] and shown in Figure 2). Each defect is modelled in a $2 \times 2 \times 2$ supercell, obtained by expanding the primitive unit cell, with a corresponding defect concentration of 1.56% and 2.08% for impurities occurring on the Cu site and O site, respectively (as a result of the unequal number of Cu and O atoms in the unit cell).

The formation energy of a defect X in charge state q is defined as [50, 51]:

$$E^f[X^q] = E_{\text{tot}}[X^q] - E_{\text{tot}}[\text{bulk}] - \sum_i n_i \mu_i + q(E_F + \varepsilon_{\text{VBM}}^{\text{H}}) + E_{\text{corr}}. \quad (2)$$

$E_{\text{tot}}[X]$ is the total energy derived from a supercell calculation containing the defect X , and $E_{\text{tot}}[\text{bulk}]$ is the total energy for the perfect crystal using an equivalent supercell. The integer n_i indicates the number of atoms of type i (host atoms or impurity atoms) that have been added to ($n_i > 0$) or removed from ($n_i < 0$) the supercell to form the defect, and μ_i are the corresponding chemical potentials of the considered species (related through $\Delta\mu_i = \mu_i - \mu_i^\circ$, where μ_i° is the chemical potential of the element i in its standard phase). The chemical potentials represent the energy of the reservoirs with which atoms are being exchanged. E_F represents the electron chemical potential, which ranges from the valence to the conduction band edges, $\varepsilon_{\text{VBM}}^{\text{H}}$ is the eigenvalue of the valence band maximum of the pristine bulk material. Finally, E_{corr} is a correction term that accounts for finite-size effects in the calculations of charged defects as well as alignment of the band edges between the bulk and the defective supercells, performed using the `SXDEFECTALIGN` code by Freysoldt *et al* [52]. The thermodynamic transition levels (ionization levels) of a given defect, $\varepsilon(q_1/q_2)$, correspond to the Fermi-level position at which a given defect changes from one charge state (q_1) to another (q_2):

$$\varepsilon(q_1/q_2) = \frac{E^f[X^{q_1}] - E^f[X^{q_2}]}{q_2 - q_1}. \quad (3)$$

The allowed values of $\Delta\mu_i$ are determined from a set of thermodynamic limits. The upper limit is given by $\Delta\mu_i \leq 0$ where element i precipitates to its standard state, e.g., $\text{O}_2(\text{g})$ (referred to half of the total energy of an oxygen molecule) and $\text{Cu}(\text{s})$. Furthermore, to avoid the formation of secondary solid phases, the chemical potentials must also be bound by:

$$2\Delta\mu_{\text{Cu}} + \Delta\mu_{\text{O}} \leq \Delta H_f(\text{Cu}_2\text{O}), \quad (4)$$

$$\Delta\mu_{\text{Cu}} + \Delta\mu_{\text{O}} \leq \Delta H_f(\text{CuO}) \quad (5)$$

with ΔH_f being the standard enthalpy of formation at zero K. The total energies of the phases competing with Cu_4O_3 , i.e., Cu_2O and CuO , were calculated using their respective unit cells. Cu_2O was modelled in a simple cubic non-magnetic cell, while for

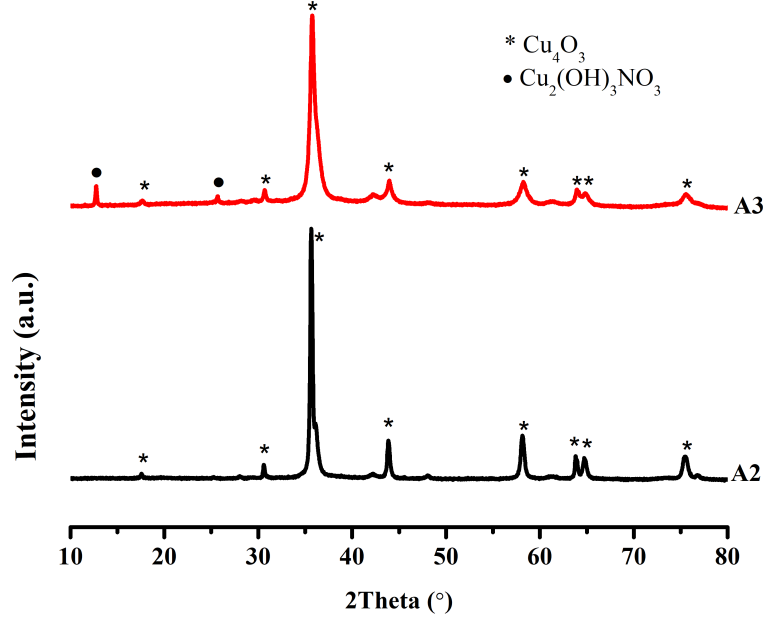


Figure 3: XRD patterns of Cu_4O_3 (A2 sample) and Cu_4O_3 with traces of $\text{Cu}_2(\text{OH})_3\text{NO}_3$ (A3 sample).

239 monoclinic CuO , a magnetic simulation cell containing 16 atoms was used together with
 240 the antiferromagnetic spin ordering leading to the observed lowest energy configuration
 241 [53, 54].

242 3 Results and discussion

243 **Structural properties and optical measurements** The crystal structure and phase
 244 purity of the products were characterized by XRD. The XRD patterns of A2 and A3
 245 are shown in Figure 3. All diffraction peaks of A2 are indexed to tetragonal Cu_4O_3
 246 (COD-9000603), which is consistent with previously reported pure Cu_4O_3 [5, 9, 12]. The
 247 diffraction peaks of A3 are in good agreement with COD-2106291. The XRD patterns
 248 of both products were found to exhibit Cu_4O_3 nature. However, the XRD pattern of the
 249 A3 sample shows, together with the already identified Cu_4O_3 an additional peak at $2\theta =$
 250 12.76° which corresponds to an intermediate phase $\text{Cu}_2(\text{OH})_3\text{NO}_3$ (COD-9008310). The
 251 existence of intermediate precursor phase $\text{Cu}_2(\text{OH})_3\text{NO}_3$ registered in the XRD pattern of
 252 the prepared A3 sample is due to the incomplete decomposition of the starting material
 253 $\text{Cu}(\text{NO}_3)_2 \cdot 3\text{H}_2\text{O}$ [5, 55]. The diffraction peaks of A2 and A3 are sharp and strong in
 254 intensity, without any other obvious impurity peaks, indicating high crystallinity and
 255 purity.

256 The average crystallite size (D) for the samples was obtained from main peaks and
 257 was calculated using the Debye-Scherrer formula:

$$D = \frac{k\lambda}{\beta \cos \theta}, \quad (6)$$

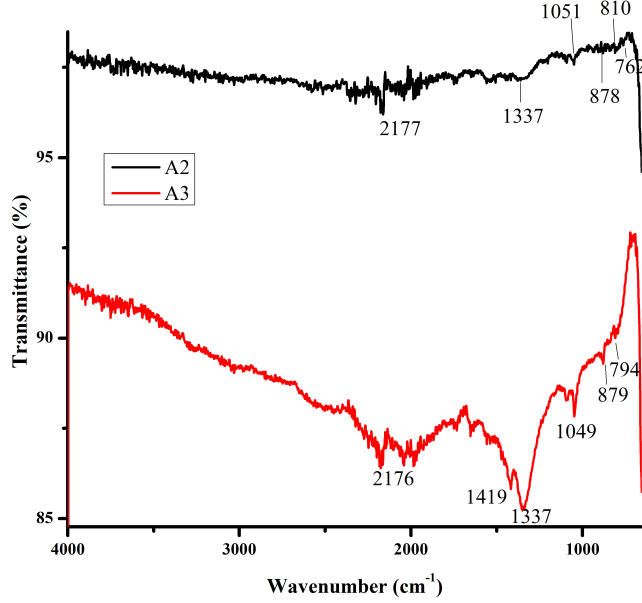
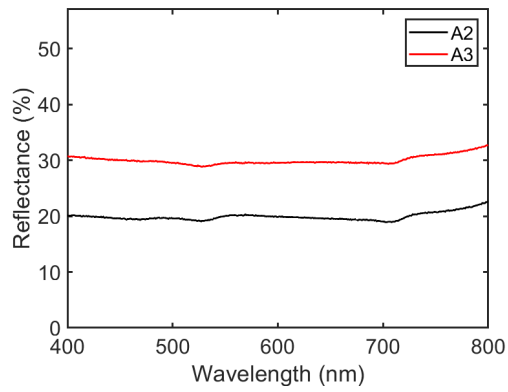


Figure 4: FT-IR spectra of Cu_4O_3 (A2 sample) and Cu_4O_3 with traces of $\text{Cu}_2(\text{OH})_3\text{NO}_3$ (A3 sample).

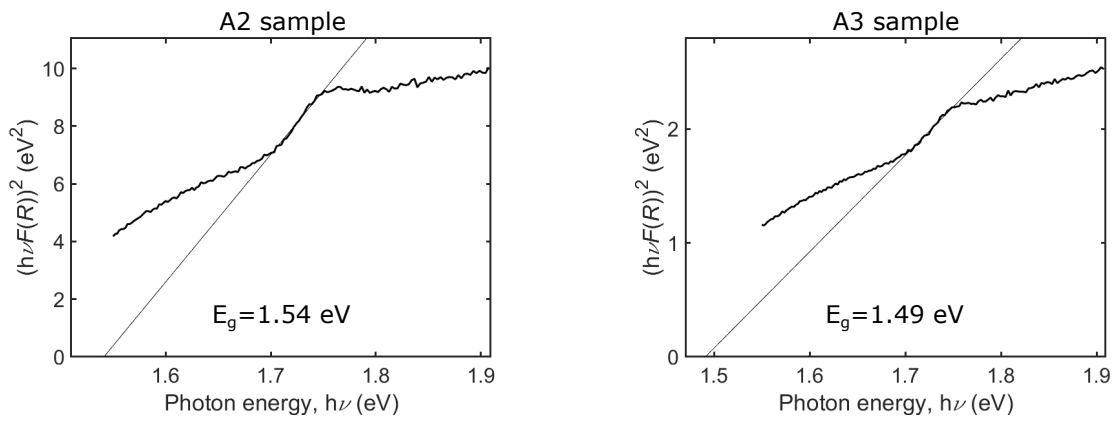
258 where D is the crystallite size, k the shape factor, λ the wavelength of the X-ray beam, θ
 259 the diffraction angle, and β the full width at half maximum (FWHM) of the peak in the
 260 XRD pattern. The calculated crystallite size of the A2 and A3 samples was found to be
 261 27.7 nm and 6.9 nm, respectively, indicating that the synthesized powders are made up
 262 of nano-particles.

263 Figure 4 shows the FT-IR spectra of Cu_4O_3 and Cu_4O_3 with $\text{Cu}_2(\text{OH})_3\text{NO}_3$ nanopow-
 264 ders. The bands below 1000 cm^{-1} can be observed in both spectra, which are assigned to
 265 the Cu–O vibration modes of Cu_4O_3 [9, 19, 16, 56]. The bands observed at 1049 cm^{-1} ,
 266 1051 cm^{-1} , 2176 cm^{-1} , and 2177 cm^{-1} are related to C–H bending and stretching [9, 56].
 267 The band at 1337 cm^{-1} was ascribed to O–H vibrations of adsorbed water (moisture) and
 268 hydroxyls in the structure of the A3 sample [9], while the band at 1419 cm^{-1} in the A3
 269 spectrum may be due to the stretching vibrations of NO_3^- [57].

270 UV-Vis diffuse reflectance spectroscopy was used to investigate the optical properties
 271 of the samples (Figure 5a). The Tauc plots obtained from the UV-Vis diffuse reflectance
 272 measurements are shown in Figure 5b. By plotting $(h\nu F(R))^2$ as a function of energy, a
 273 line of best fit through the point of maximum gradient within each Tauc plot, the direct
 274 optical band gaps were determined to be 1.54 eV and 1.49 eV for Cu_4O_3 and $\text{Cu}_4\text{O}_3 +$
 275 $\text{Cu}_2(\text{OH})_3\text{NO}_3$, respectively. The band gap of A2 is within the range of the band gap
 276 of the previously synthesized Cu_4O_3 [19, 58, 20, 7]. From the Tauc plots, none of the
 277 data sets appear to produce a typical plot as there are multiple absorption steps in each
 278 case. Such Tauc plots confirm the presence of mixed valence copper ions present in the
 279 A2 sample, while in the case of the A3 sample they are the consequence of the compound
 280 mixture. However, the most notable step was fitted to obtain the band gaps.



(a)



(b)

Figure 5: Diffuse reflectance spectra of the A2 and A3 samples in (a), together with the corresponding Tauc plots in (b).

Table 3: Calculated enthalpies of formation (eV/formula unit) for Cu_4O_3 . Values for Cu_2O and CuO are shown for validation of values within a used functional.

	ΔH_f (Cu_2O)	ΔH_f (Cu_4O_3)	ΔH_f CuO
HSE06	-1.66	-4.92	-1.57
SC-B3LYP	-2.21	-5.32	-1.69
	-1.75 [59]	-4.69 (at 427° C) [60]	-1.59 [59]
Experiment		-4.88 (at 25° C) [60]	
		-5.94 \pm 25 (at 25° C) [60]	

281 **Electronic properties** As demonstrated in previous works concerning the modelling
282 of bulk Cu_4O_3 [17, 26], local and semi-local DFT was found unsatisfactory for the descrip-
283 tion of its electronic properties. Hybrid-DFT, in the form of HSE06, captures the correct
284 nature of the first band-to-band transition as indirect, but produces a difference between
285 the indirect and direct band gap which underestimates experimental values. By tuning
286 the exact exchange within HSE06, the electronic structure is influenced only by lower-
287 ing the position of the conduction band relative to the valence band, hence decreasing
288 the band gap value without significantly altering its structure (as outlined in an earlier
289 work [48]). However, since there are many other available approximations for the XC
290 functional, the question arises whether another functional can accurately reproduce the
291 electronic properties of Cu_4O_3 or whether this material cannot be modelled accurately by
292 DFT? Unlike HSE06, B3LYP is a global functional, where the amount of HF exchange
293 included does not depend on the distance between electrons. In order to test the accu-
294 racy of a different type of hybrid functional, B3LYP was used to calculate the electronic
295 properties of Cu_4O_3 . The calculated electronic structure using the self-consistently de-
296 termined optimal fraction for B3LYP (SC-B3LYP) is shown in Figure 6. The obtained
297 SC-B3LYP indirect and direct band gaps read 1.89 eV and 2.41 eV for the ground state
298 antiferromagnetic ordering. This value is somewhat higher than the experimentally noted
299 gap for the pure A2 sample. However, for a ferromagnetic ground state of Cu_4O_3 , a di-
300 rect band gap of 1.44 eV is found, indicating that the temperature-induced rearrangement
301 of the spin order may influence the electronic structure significantly, similar to what is
302 observed in CuO [53].

303 **Phase stability** Calculated formation enthalpies of Cu_4O_3 are reported in Table 3.
304 Both HSE06 (with standard 20% exact exchange) and SC-B3LYP show similar trends
305 with results being reasonably close to experimental values. The slight overestimation
306 of SC-B3LYP values is not necessarily a surprise, since it is known that the B3LYP
307 functional does not provide accurate total energies for metallic Cu, as demonstrated in
308 earlier works [61]. Limits for the chemical potential range valid for pristine Cu_4O_3 were

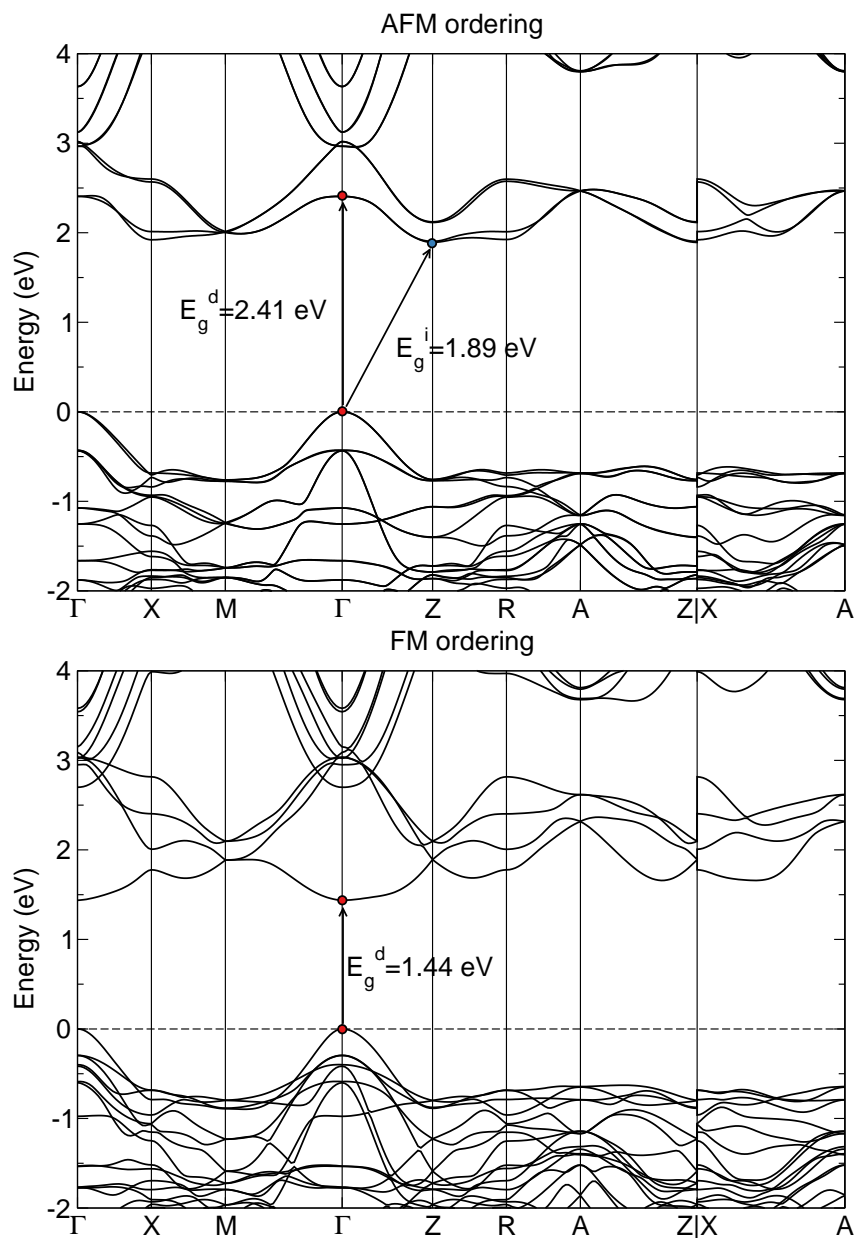


Figure 6: Computed electronic band structure of Cu_4O_3 for two different magnetic orderings using SC-B3LYP, where the fraction of exact exchange was obtained in a self-consistent manner. The dashed line indicates the highest occupied valence state.

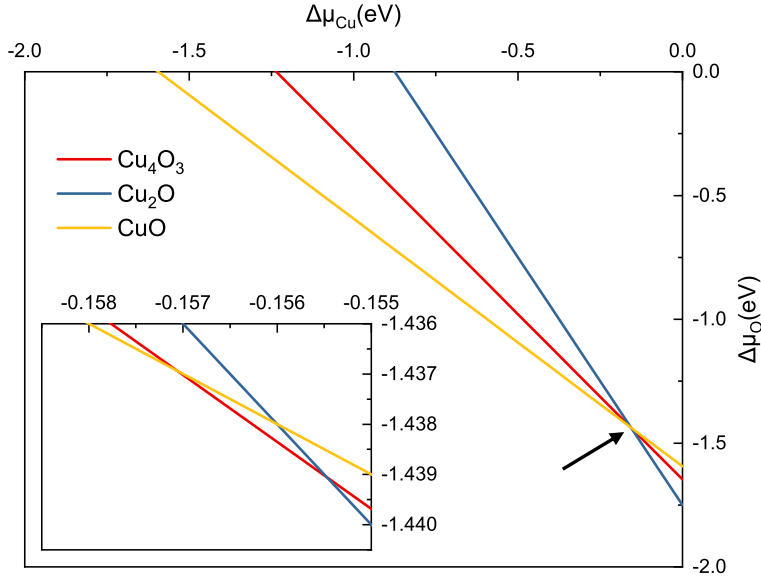


Figure 7: Phase stability in the range of accessible chemical potentials for Cu_4O_3 , constructed from available experimental data. Limits are imposed by the formation of competing phases, i.e., Cu_2O and CuO . The black arrow denotes the narrow stability region of Cu_4O_3 , emphasized further in the zoom-in plot.

309 calculated from available formation enthalpies and constraints set by the evolution of
 310 competing phases, in this case Cu_2O and CuO .

311 In order to bypass stability issues originating from the use of different functionals,
 312 values for formation enthalpies entering the stability range calculation were taken from
 313 available experimental data. The calculated phase stability region for Cu_4O_3 is shown
 314 in Figure 7. The thermodynamic stability window of Cu_4O_3 is narrow, in accord with
 315 the observed difficulty of synthesizing pure samples without Cu_2O or CuO being present.
 316 Effectively, Cu_4O_3 can only be created under Cu-rich/O-poor conditions, with chemical
 317 potential values reading $\Delta\mu_{\text{Cu}} = -0.157 \text{ eV}$ and $\Delta\mu_{\text{O}} = -1.437 \text{ eV}$. Furthermore, the
 318 observed narrowness of the available stability region for Cu_4O_3 indicates that the choice
 319 of functional would not substantially alter the defect formation energies, calculated at
 320 this specific point in chemical potential space.

321 As outlined previously, Cu_4O_3 contains two distinct Cu and O atoms. They can be
 322 distinguished through their coordination number or oxidation (valence) state. The first
 323 one (Cu^{1+}) is a cuprous Cu binding two nearest neighbouring O atoms (labelled O-1)
 324 in a linear arrangement, while the other (Cu^{2+}) is a cupric Cu surrounded by four O
 325 atoms in an almost square planar configuration. Each O atom, on the other hand, binds
 326 four Cu atoms, with the difference that the first (O-1) binds four Cu^{2+} atoms while the
 327 second (O-2) binds two Cu^{1+} and two Cu^{2+} atoms. The Bader charge analysis provides
 328 a useful way of determining those differences in order to detect distinct impurity sites
 329 within the cell. Results for clean Cu_4O_3 are presented in Table 4. Despite the nominal

Table 4: Bader charge analysis of Cu_4O_3 using three different approximations for the XC functional. Values reported in e^- .

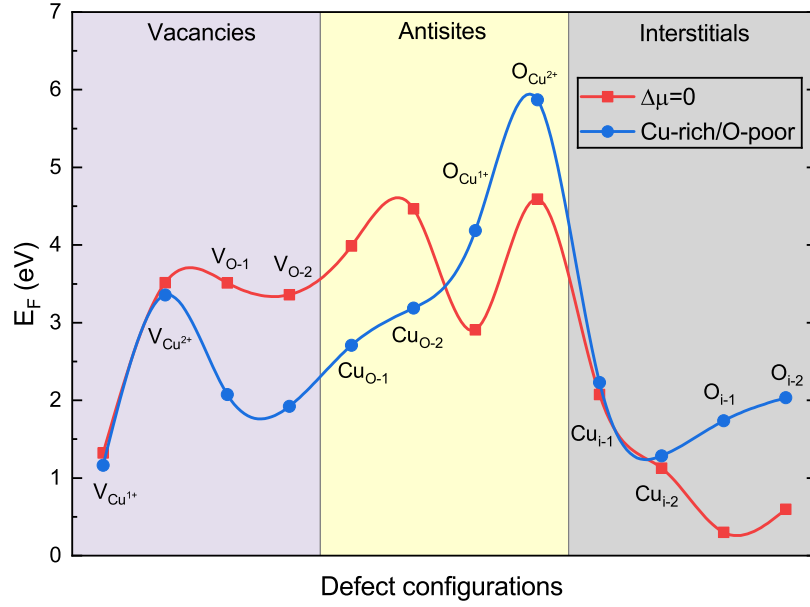
	Cu^{1+}	Cu^{2+}	O-1	O-2
DFT+ U	+0.534	+0.913	-0.959	-0.936
HSE06	+0.563	+1.122	-1.130	-1.112
SC-B3LYP	+0.545	+1.070	-1.089	-1.065

charge state of -2 , the two O atoms show small differences in accumulated charge of $\Delta = 0.02 e^-$, regardless of the chosen functional approximation. Interestingly, DFT+ U results follow the same trend as HSE06 and SC-B3LYP ones, with absolute values being considerably reduced. However, results presented in the following paragraphs consider mostly SC-B3LYP results, owing to the accurate description of the initial electronic structure. Comparison with DFT+ U or HSE06 results is drawn where appropriate. Following the outlined analysis, it is noted that vacancy and antisite defects modelled in Cu_4O_3 include two distinct configurations in order to capture all possible sites.

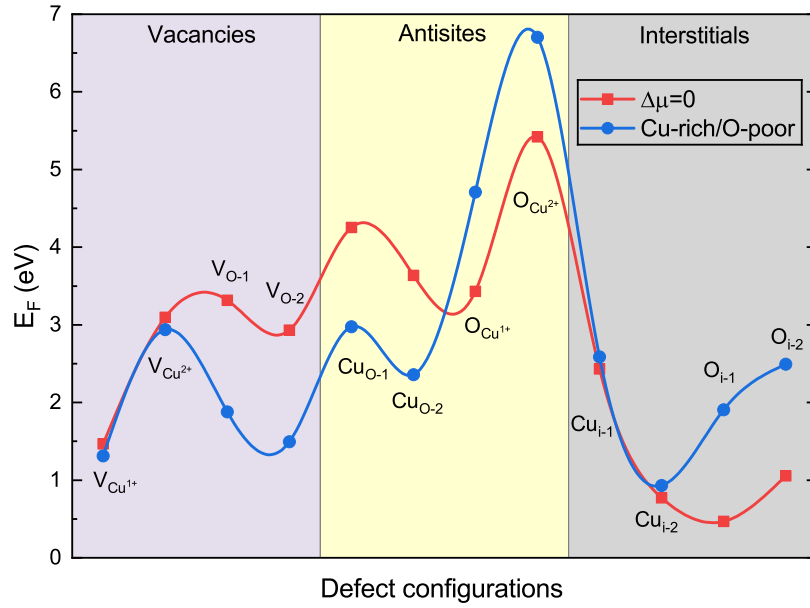
Intrinsic defects The calculated formation energies of simple neutral defects in Cu_4O_3 are presented in Figure 8, with vacancies shown on the left hand side. The two Cu vacancies, corresponding to the removal of one Cu^{1+} or Cu^{2+} atom are labelled as $V_{\text{Cu}^{1+}}$ and $V_{\text{Cu}^{2+}}$, respectively, while the two O vacancies are named $V_{\text{O-1}}$ and $V_{\text{O-2}}$ distinguishing between the sites identified earlier. Note how the calculated defect formation energies do not depend greatly on the functional approximation, retaining overall trends. This points towards the applicability of DFT+ U calculations as an affordable approach for pre-screening of defects, while finer formation energy distributions should be obtained using a hybrid functional.

Removing a Cu^{1+} atom from the crystal lattice results in two dangling bonds from the neighbouring O atoms with mostly p character. The formation of a neutral $V_{\text{Cu}^{1+}}$ defect causes the two closest O atoms to relax away from the site, yet the overall influence on the lattice parameters is less than 0.8% expansion. A neutral $V_{\text{Cu}^{1+}}$ defect creates a singly-unoccupied state in the otherwise empty electronic band structure (see Figure 9). The unoccupied acceptor level is located around 0.66 eV above the VB maximum in the spin majority channel, originating mainly from Cu d and O p states. The created hole is highly delocalized in real space (not shown explicitly). As the defect becomes occupied in the -1 charge state, no further relaxation effects are noted and the excess charge is readily incorporated into the lattice. $V_{\text{Cu}^{1+}}$ is a shallow acceptor in Cu_4O_3 (see Figure 10), existing as a charged defect across the whole range of available Fermi levels, with the $\varepsilon(0/-1)$ transition level located inside the valence band maximum (VBM).

The cost to create a neutral $V_{\text{Cu}^{2+}}$ is much higher than that of a neutral $V_{\text{Cu}^{1+}}$, which is



(a) DFT+U



(b) SC-B3LYP

Figure 8: Formation energy of all native defects occurring in Cu_4O_3 in the charge neutral state. Results are presented for two different approximation for the XC functional as well as two distinct chemical potential limits. The red line illustrates the maximally Cu- and O-rich conditions ($\Delta\mu_i = 0$), while the blue line represents the only stability point of Cu_4O_3 discussed earlier. The actual values are represented with filled symbols, while the lines are visual guidelines.

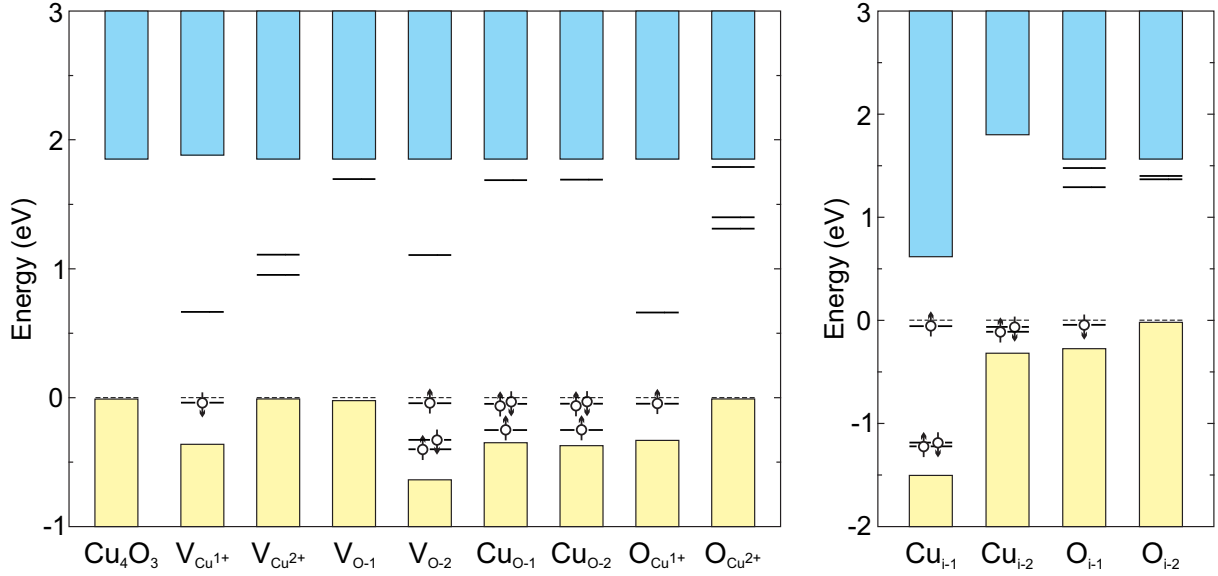


Figure 9: Schematic representation of the electronic densities of states of clean and defective Cu_4O_3 in their respective charge neutral state. The dashed line indicates the highest occupied band and up/down arrows represent different spin channels.

360 anticipated as it essentially describes the energy required to break the four $\text{Cu}^{2+}\text{-O}$ bonds
 361 (compared to two $\text{Cu}^{1+}\text{-O}$ ones). The removal of a Cu^{2+} atom leads to a relaxation of the
 362 nearest O atoms away from the defect site, similar to the $\text{V}_{\text{Cu}^{1+}}$ defect. The neighbouring
 363 O atoms relax towards each other, alternating the O-O distance for $0.02\text{-}0.05 \text{ \AA}$, in
 364 order to maximize their bond overlap. When the $\text{V}_{\text{Cu}^{2+}}$ defect becomes populated, the
 365 ions relax slightly further away from the defect site due to increased Coulomb repulsion.
 366 The $\varepsilon(0/-1)$ ionization level is found inside VBM, whereas the $\varepsilon(-1/-2)$ transition
 367 acts as a deep acceptor located 0.47 eV above the VBM.

368 Removing one O-1 or O-2 atom leaves the two electrons from the surrounding Cu
 369 atoms weakly bound to their respective hosts. The doubly unoccupied defect states
 370 are localized well below the conduction band minimum (CBM), resulting in a lattice
 371 relaxation in order to accommodate the defect. Both $\text{V}_{\text{O-1}}$ and $\text{V}_{\text{O-2}}$ are stable as neutral
 372 defects, with the corresponding ionization levels well inside the valence band, indicating
 373 that they do not act as charge compensating defects in Cu_4O_3 .

374 Antisite defects in Cu_4O_3 are unlikely to form due to their high formation energies.
 375 Moreover, $\text{Cu}_{\text{O-1}}$ and $\text{Cu}_{\text{O-2}}$ exist as neutral defects over the entire Fermi level range and,
 376 similar to O vacancies do not participate in charge compensating phenomena. $\text{O}_{\text{Cu}^{1+}}$ and
 377 $\text{O}_{\text{Cu}^{2+}}$ are stable in the -1 charged state with the $\text{O}_{\text{Cu}^{1+}}$ possessing a deep $\varepsilon(-1/-2)$
 378 transition level at 1.53 eV above the VBM, while the same $\varepsilon(-1/-2)$ for $\text{O}_{\text{Cu}^{2+}}$ is located
 379 inside the CBM.

380 Out of the three suitable positions for interstitial atoms (shown earlier in Figure 2),
 381 i-2 and i-3 relax to yield identical behaviour due to symmetry of the lattice site where the
 382 defect is incorporated. $\text{Cu}_{\text{i-1}}$ is found to incorporate into the plane of zig-zag Cu^{1+} atoms,

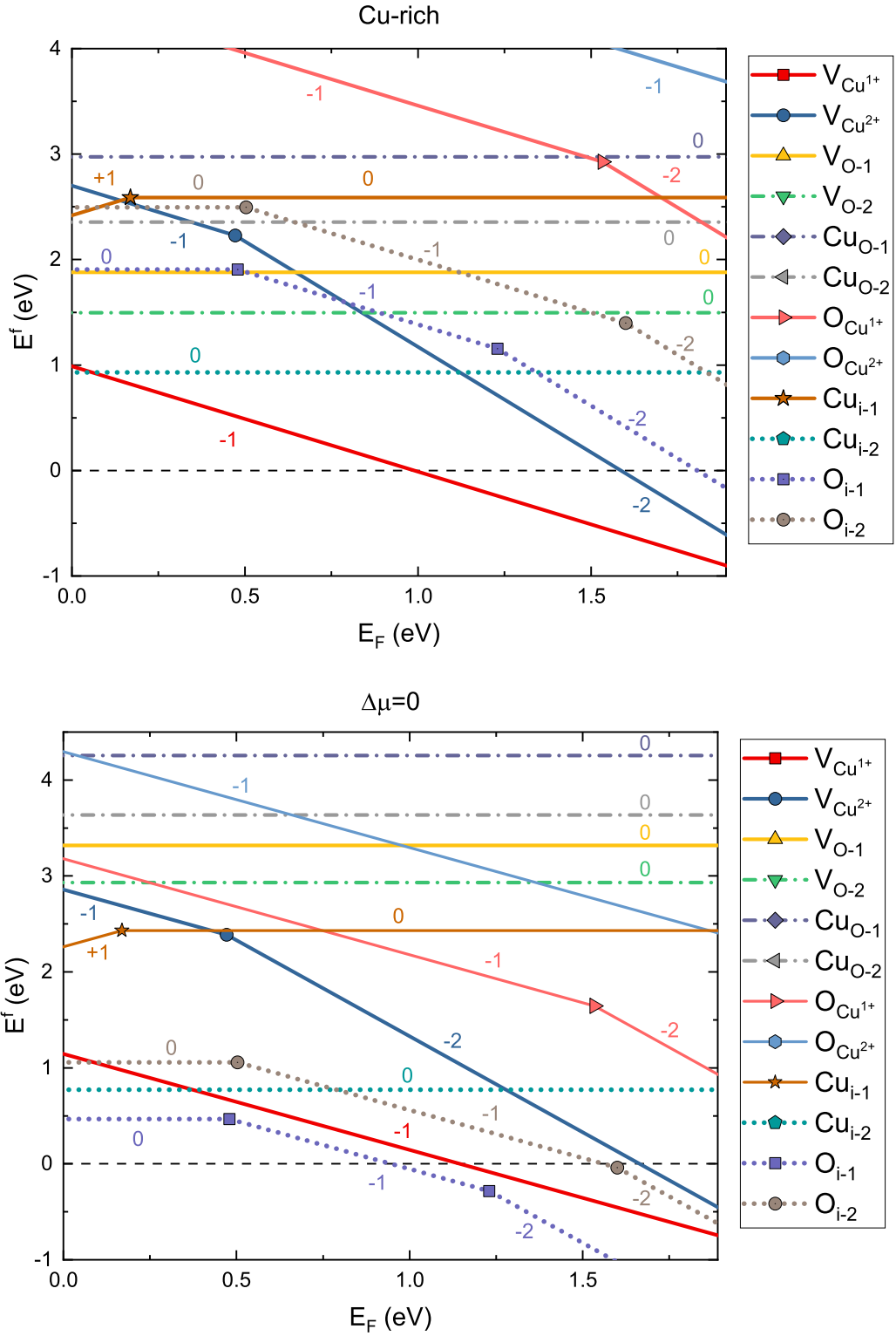


Figure 10: Formation energy of native charged defects occurring in Cu_4O_3 , plotted as a function of the Fermi level varying from the top of the valence band maximum to the bottom of the conduction band minimum, under conditions chosen in Figure 9. The slope of the lines denotes the charge state and the solid dots represent the transition levels ϵ .

383 causing the neighbouring Cu atom to relax away from the similarly charged interstitial
 384 site. Cu_{i-1} behaves as a relatively shallow donor, with a $\varepsilon(+1/0)$ ionization level at
 385 approximately 0.17 eV above the VBM. However, the formation energy of the Cu_{i-1} defect
 386 lies relatively high around 2.5 eV, compared to other defects available in Cu_4O_3 . On the
 387 other hand, the formation energy of neutral Cu_{i-2} is approximately 1 eV, where a simple
 388 lattice rearrangement allows the interstitial to fully bind onto its neighbouring O atoms.
 389 Cu_{i-2} is found in the neutral charge state across the whole Fermi level range, with the
 390 $\varepsilon(+1/0)$ thermodynamic transition located well in the VBM.

391 Interstitial O incorporated in position 1, O_{i-1} , binds actively to nearest neighbouring
 392 Cu atoms, inducing a charge transfer process, with a Bader charge value of $-0.96 e^-$
 393 being very close to $-1.08 e^-$ found on a O atom located far away from the defect site.
 394 O_{i-1} acts as a deep acceptor in Cu_4O_3 , with the transition levels $\varepsilon(0/-1)$ and $\varepsilon(-1/-2)$
 395 located 0.48 eV and 1.23 eV above the VBM. O_{i-2} is found to behave in a similar manner
 396 to O_{i-1} , with the $\varepsilon(0/-1)$ and $\varepsilon(-1/-2)$ ionization levels 0.50 eV and 1.60 eV above the
 397 VBM, respectively.

398 **Trends in formation energies** Altogether, there is a complex interplay between the
 399 formation of defects and conditions under which they are formed in Cu_4O_3 . From the
 400 obtained plot of the formation energy as a function of the Fermi-level position for all
 401 intrinsic defects, $V_{\text{Cu}^{1+}}$ is the lowest energy acceptor defect for Cu_4O_3 created under
 402 Cu-rich conditions. It should also be noted that the formation energy of neutral Cu_{i-2}
 403 is 0.05 eV lower than that of negatively charged $V_{\text{Cu}^{1+}}$, although for a very small range
 404 of Fermi levels around the VBM. However, the ionization levels of Cu_{i-2} are deep in
 405 the valence band, indicating that Cu_{i-2} will not act as an effective hole compensating
 406 defect. Hence, Cu_4O_3 grown under the narrow span of available conditions will be a
 407 *p*-type semiconductor in nature. Moreover, there are almost no intrinsic *n*-type defects
 408 present to play a large role in the conductivity of Cu_4O_3 . Finally, the formation energies
 409 of neither oxygen vacancies nor oxygen interstitials are found low enough to drive the
 410 conversion of Cu_4O_3 towards Cu_2O or CuO , respectively, as discussed when analysing the
 411 stoichiometry of paramelaconite earlier in the introduction.

412 The power of the computational approaches to materials modelling is that one can
 413 modify individual parameters and observe their effect on certain properties. In this
 414 case, the growth conditions were altered through the corresponding chemical potential
 415 to study the behaviour of Cu_4O_3 under rather unphysical conditions which favour the
 416 formation of CuO or Cu_2O . The calculated formation energies under equal chemical
 417 potential limits (Cu-rich/O-rich, where $\Delta\mu_i = 0$) is shown in Figure 10. In this case
 418 the O_{i-1} becomes the dominant defect in Cu_4O_3 , with a neutral formation energy of
 419 only 0.5 eV, which is low enough to cause structural instability (oxidation) towards the
 420 formation of CuO . Furthermore, O_{i-1} has two acceptor transitions deep inside the band

421 gap, worsening drastically the p -type conductivity compared to Cu_4O_3 formed under
422 Cu-rich conditions.

423 4 Conclusion

424 The ground state properties and native point defects of Cu_4O_3 were modelled using den-
425 sity functional theory calculations. The stability region of Cu_4O_3 was assessed, depending
426 on the varying chemical potentials of constituting species. Based on the analysis outlined,
427 several significant findings were identified:

- 428 • Global range hybrid functionals outperform their range-separated analogues in the
429 case of Cu_4O_3 , where results close to experimental ones were obtained using B3LYP-
430 based calculations with a self-consistently determined amount of exact exchange
431 within.
- 432 • Cu_4O_3 is found to be thermodynamically stable in a very narrow range of accessible
433 chemical potentials. This corroborates the experimentally noted sensitivity upon
434 synthesis conditions.
- 435 • Under the observed growth conditions (Cu-rich), Cu_4O_3 demonstrates good intrinsic
436 p -type conductivity arising from vacancy defects readily occurring on the Cu^{1+}
437 atomic site.
- 438 • Intrinsic defects are not a source of n -type conductivity in Cu_4O_3 because they are
439 unable to act as shallow donors or to compensate p -type conductivity.

440 However, whilst interpreting results outlined in this work, several limitations apply. Ther-
441 modynamic stability conditions as well as defect related properties (formation energies,
442 migration barriers, etc.) depend on temperature effects, whose extent is inaccessible
443 within the given theoretical framework. Despite those obvious constraints, the results
444 obtained provide insights into difficulties related to obtaining pure Cu_4O_3 and main-
445 taining it stable over longer periods of time, further exemplified by the experimental
446 difficulties in synthesising phase-pure Cu_4O_3 samples.

447 Acknowledgements

448 We acknowledge the Cardiff University School of Chemistry for a PhD studentship for
449 AŽ and the Royal Society DfID Africa programme for funding. NYD acknowledges the
450 UK Engineering and Physical Sciences Research Council (EPSRC) for funding (Grant
451 No. EP/S001395/1). This work was performed using the computational facilities of the
452 Advanced Research Computing @ Cardiff (ARCCA) Division, Cardiff University. Via

our membership of the UK’s HPC Materials Chemistry Consortium, which is funded by EPSRC (EP/L000202), this work made use of the ARCHER facility, the UK’s national high-performance computing service, which is funded by the Office of Science and Technology through EPSRC’s High End Computing Programme.

References

- [1] C. Frondel, “Paramelaconite: A tetragonal oxide of copper,” *American Mineralogist*, vol. 26, pp. 657–672, nov 1941.
- [2] N. Datta and J. W. Jeffery, “The crystal structure of paramelaconite, $\text{Cu}_{12}^{2+}\text{Cu}_4^+\text{O}_{14}$,” *Acta Crystallographica Section B*, vol. 34, pp. 22–26, jan 1978.
- [3] M. O’Keeffe and J.-O. Bovin, “The crystal structure of paramelaconite, Cu_4O_3 ,” *American Mineralogist*, vol. 63, pp. 180–185, 1978.
- [4] P. E. Morgan, D. E. Partin, B. L. Chamberland, and M. O’Keeffe, “Synthesis of paramelaconite: Cu_4O_3 ,” *Journal of Solid State Chemistry*, vol. 121, no. 1, pp. 33–37, 1996.
- [5] L. Zhao, H. Chen, Y. Wang, H. Che, P. Gunawan, Z. Zhong, H. Li, and F. Su, “Facile Solvothermal Synthesis of Phase-Pure Cu_4O_3 Microspheres and Their Lithium Storage Properties,” *Chemistry of Materials*, vol. 24, no. 6, pp. 1136–1142, 2012.
- [6] N. J. Long and A. K. Petford-Long, “In-situ electron-beam-induced reduction of CuO : A study of phase transformations in cupric oxide,” *Ultramicroscopy*, vol. 20, no. 1-2, pp. 151–159, 1986.
- [7] J. F. Pierson, A. Thobor-Keck, and A. Billard, “Cuprite, paramelaconite and tenorite films deposited by reactive magnetron sputtering,” *Applied Surface Science*, vol. 210, no. 3-4, pp. 359–367, 2003.
- [8] D. S. Murali and S. Aryasomayajula, “Thermal conversion of Cu_4O_3 into CuO and Cu_2O and the electrical properties of magnetron sputtered Cu_4O_3 thin films,” *Applied Physics A*, vol. 124, p. 279, mar 2018.
- [9] W. Wang, L. Zhu, P. Lv, G. Liu, Y. Yu, and J. Li, “Novel Candy-like Cu_4O_3 Microstructure: Facile Wet Chemical Synthesis, Formation Mechanism, and Good Long-Term Antibacterial Activities,” *ACS Applied Materials & Interfaces*, vol. 10, pp. 37287–37297, oct 2018.

- 483 [10] N. Martić, C. Reller, C. Macauley, M. Löffler, B. Schmid, D. Reinisch, E. Volkova,
484 A. Maltenberger, A. Rucki, K. J. J. Mayrhofer, and G. Schmid, “Paramelaconite-
485 Enriched Copper-Based Material as an Efficient and Robust Catalyst for Electro-
486 chemical Carbon Dioxide Reduction,” *Advanced Energy Materials*, vol. 9, p. 1901228,
487 aug 2019.
- 488 [11] M. A. M. Patwary, C. Y. Ho, K. Saito, Q. Guo, K. M. Yu, W. Walukiewicz, and
489 T. Tanaka, “Effect of oxygen flow rate on properties of Cu_4O_3 thin films fabricated by
490 radio frequency magnetron sputtering,” *Journal of Applied Physics*, vol. 127, no. 8,
491 2020.
- 492 [12] H. S. Kim, P. Yadav, M. Patel, J. Kim, K. Pandey, D. Lim, and C. Jeong, “Transpar-
493 ent $\text{Cu}_4\text{O}_3/\text{ZnO}$ heterojunction photoelectric devices,” *Superlattices and Microstruc-
494 tures*, vol. 112, pp. 262–268, 2017.
- 495 [13] L. Pinsard-Gaudart, J. Rodríguez-Carvajal, A. Gukasov, and P. Monod, “Magnetic
496 properties of paramelaconite (Cu_4O_3) : A pyrochlore lattice with $S=\frac{1}{2}$,” *Physical
497 Review B*, vol. 69, p. 104408, mar 2004.
- 498 [14] D. Djurek, M. Prester, D. Drobac, M. Ivanda, and D. Vojta, “Magnetic properties
499 of nanoscaled paramelaconite $\text{Cu}_4\text{O}_{3-x}$ ($x=0.0$ and 0.5),” *Journal of Magnetism and
500 Magnetic Materials*, vol. 373, pp. 183–187, jan 2015.
- 501 [15] E. M. Tejada-Rosales, J. Rodríguez-Carvajal, N. Casañ-Pastor, P. Alemany, E. Ruiz,
502 M. S. El-Fallah, S. Alvarez, and P. Gómez-Romero, “Room-Temperature Synthesis
503 and Crystal, Magnetic, and Electronic Structure of the First Silver Copper Oxide,”
504 *Inorganic Chemistry*, vol. 41, pp. 6604–6613, dec 2002.
- 505 [16] L. Debbichi, M. C. Marco de Lucas, J. F. Pierson, and P. Kruger, “Vibrational prop-
506 erties of CuO and Cu_4O_3 from first-principles calculations, and raman and infrared
507 spectroscopy,” *The Journal of Physical Chemistry C*, vol. 116, pp. 10232–10237,
508 2012.
- 509 [17] M. Heinemann, B. Eifert, and C. Heiliger, “Band structure and phase stability of
510 the copper oxides Cu_2O , CuO , and Cu_4O_3 ,” *Physical Review B*, vol. 87, p. 115111,
511 mar 2013.
- 512 [18] L. Debbichi, M. C. Marco de Lucas, and P. Krüger, “Electronic structure, lattice
513 dynamics and thermodynamic stability of paramelaconite Cu_4O_3 ,” *Materials Chem-
514 istry and Physics*, vol. 148, pp. 293–298, nov 2014.
- 515 [19] D. S. Murali and A. Subrahmanyam, “Synthesis of low resistive p type Cu_4O_3 thin
516 films by DC reactive magnetron sputtering and conversion of Cu_4O_3 into CuO by

- 517 laser irradiation,” *Journal of Physics D: Applied Physics*, vol. 49, no. 37, p. 375102,
518 2016.
- 519 [20] D. Reppin, A. Polity, B. Meyer, and S. Shokovets, “Optical and electrical properties
520 of Cu_2O , Cu_4O_3 and CuO ,” *Mater. Res. Soc. Symp. Proc. Vol.*, vol. 1494, no. x,
521 pp. 25–31, 2012.
- 522 [21] Y. Wang, S. Lany, J. Ghanbaja, Y. Fagot-Revurat, Y. P. Chen, F. Soldera, D. Hor-
523 wat, F. Mücklich, and J. F. Pierson, “Electronic structures of Cu_2O , Cu_4O_3 , and
524 CuO : A joint experimental and theoretical study,” *Physical Review B*, vol. 94,
525 p. 245418, dec 2016.
- 526 [22] G. Kresse and D. Joubert, “From ultrasoft pseudopotentials to the projector
527 augmented-wave method,” *Physical Review B*, vol. 59, pp. 1758–1775, jan 1999.
- 528 [23] P. E. Blöchl, “Projector augmented-wave method,” *Physical Review B*, vol. 50,
529 pp. 17953–17979, dec 1994.
- 530 [24] J. P. Perdew, K. Burke, and M. Ernzerhof, “Generalized Gradient Approximation
531 Made Simple,” *Physical Review Letters*, vol. 77, no. 18, pp. 3865–3868, 1996.
- 532 [25] S. L. Dudarev, G. A. Botton, S. Y. Savrasov, C. J. Humphreys, and a. P. Sut-
533 ton, “Electron-energy-loss spectra and the structural stability of nickel oxide: An
534 LSDA+U study,” *Physical Review B*, vol. 57, pp. 1505–1509, jan 1998.
- 535 [26] A. Živković, A. Roldan, and N. H. de Leeuw, “Density functional theory study ex-
536 plaining the underperformance of copper oxides as photovoltaic absorbers,” *Physical*
537 *Review B*, vol. 99, p. 035154, jan 2019.
- 538 [27] J. Heyd, G. E. Scuseria, and M. Ernzerhof, “Hybrid functionals based on a screened
539 Coulomb potential,” *The Journal of Chemical Physics*, vol. 118, pp. 8207–8215, may
540 2003.
- 541 [28] J. Heyd and G. E. Scuseria, “Efficient hybrid density functional calculations in solids:
542 Assessment of the Heyd-Scuseria-Ernzerhof screened Coulomb hybrid functional,”
543 *Journal of Chemical Physics*, vol. 121, pp. 1187–1192, jul 2004.
- 544 [29] J. Heyd, G. E. Scuseria, and M. Ernzerhof, “Erratum: “Hybrid functionals based on
545 a screened Coulomb potential” [J. Chem. Phys. 118, 8207 (2003)],” *The Journal of*
546 *Chemical Physics*, vol. 124, p. 219906, jun 2006.
- 547 [30] S. Grimme, J. Antony, S. Ehrlich, and H. Krieg, “A consistent and accurate ab
548 initio parametrization of density functional dispersion correction (DFT-D) for the
549 94 elements H-Pu,” *The Journal of Chemical Physics*, vol. 132, p. 154104, apr 2010.

- 550 [31] H. J. Monkhorst and J. D. Pack, “Special points for Brillouin-zone integrations,”
551 *Physical Review B*, vol. 13, pp. 5188–5192, jun 1976.
- 552 [32] M. I. Aroyo, J. M. Perez-Mato, C. Capillas, E. Kroumova, S. Ivantchev,
553 G. Madariaga, A. Kirov, and H. Wondratschek, “Bilbao Crystallographic Server:
554 I. Databases and crystallographic computing programs,” *Zeitschrift für Kristallographie - Crystalline Materials*, vol. 221, jan 2006.
- 556 [33] M. I. Aroyo, A. Kirov, C. Capillas, J. M. Perez-Mato, and H. Wondratschek, “Bilbao
557 Crystallographic Server. II. Representations of crystallographic point groups and
558 space groups,” *Acta Crystallographica Section A Foundations of Crystallography*,
559 vol. 62, pp. 115–128, mar 2006.
- 560 [34] M. I. Aroyo, J. M. Perez-Mato, D. Orobengoa, E. Tasci, G. De La Flor, and A. Kirov,
561 “Crystallography online: Bilbao crystallographic server,” *BULGARIAN CHEMI-
562 CAL COMMUNICATIONS*, vol. 43, no. 2, pp. 183–197, 2011.
- 563 [35] G. Pizzi, D. Volja, B. Kozinsky, M. Fornari, and N. Marzari, “BoltzWann: A
564 code for the evaluation of thermoelectric and electronic transport properties with a
565 maximally-localized Wannier functions basis,” *Computer Physics Communications*,
566 vol. 185, no. 1, pp. 422–429, 2014.
- 567 [36] G. Pizzi, V. Vitale, R. Arita, S. Blügel, F. Freimuth, G. Géranton, M. Giber-
568 tini, D. Gresch, C. Johnson, T. Koretsune, J. Ibañez-Azpiroz, H. Lee, J.-M. Lihm,
569 D. Marchand, A. Marrazzo, Y. Mokrousov, J. I. Mustafa, Y. Nohara, Y. No-
570 mura, L. Paulatto, S. Poncé, T. Ponweiser, J. Qiao, F. Thöle, S. S. Tsirkin,
571 M. Wierzbowska, N. Marzari, D. Vanderbilt, I. Souza, A. A. Mostofi, and J. R.
572 Yates, “Wannier90 as a community code: new features and applications,” *Journal
573 of Physics: Condensed Matter*, vol. 32, p. 165902, apr 2020.
- 574 [37] J. Buckeridge, D. Scanlon, A. Walsh, and C. Catlow, “Automated procedure to
575 determine the thermodynamic stability of a material and the range of chemical po-
576 tentials necessary for its formation relative to competing phases and compounds,”
577 *Computer Physics Communications*, vol. 185, pp. 330–338, jan 2014.
- 578 [38] M. Yu and D. R. Trinkle, “Accurate and efficient algorithm for Bader charge inte-
579 gration,” *The Journal of Chemical Physics*, vol. 134, p. 064111, feb 2011.
- 580 [39] W. Tang, E. Sanville, and G. Henkelman, “A grid-based Bader analysis algorithm
581 without lattice bias,” *Journal of Physics: Condensed Matter*, vol. 21, p. 084204, feb
582 2009.

- 583 [40] E. Sanville, S. D. Kenny, R. Smith, and G. Henkelman, “Improved grid-based al-
584 gorithm for Bader charge allocation,” *Journal of Computational Chemistry*, vol. 28,
585 pp. 899–908, apr 2007.
- 586 [41] K. Momma and F. Izumi, “VESTA 3 for three-dimensional visualization of crystal,
587 volumetric and morphology data,” *Journal of Applied Crystallography*, vol. 44, no. 6,
588 pp. 1272–1276, 2011.
- 589 [42] R. Dovesi, V. R. Saunders, C. Roetti, R. Orlando, C. M. Zicovich-Wilson, F. Pascale,
590 B. Civalleri, K. Doll, N. M. Harrison, I. J. Bush, P. D’Arco, M. Llunell, M. Causà,
591 Y. Noël, L. Maschio, A. Erba, M. Rerat, and S. Casassa, “CRYSTAL17 User’s
592 Manual,” 2017.
- 593 [43] R. Dovesi, A. Erba, R. Orlando, C. M. Zicovich-Wilson, B. Civalleri, L. Maschio,
594 M. Rérat, S. Casassa, J. Baima, S. Salustro, and B. Kirtman, “Quantum-mechanical
595 condensed matter simulations with CRYSTAL,” *Wiley Interdisciplinary Reviews:
596 Computational Molecular Science*, vol. 8, no. 4, pp. 1–36, 2018.
- 597 [44] J. Linnera, G. Sansone, L. Maschio, and A. J. Karttunen, “Thermoelectric Properties
598 of p-Type Cu₂O, CuO, and NiO from Hybrid Density Functional Theory,” *The
599 Journal of Physical Chemistry C*, vol. 122, pp. 15180–15189, jul 2018.
- 600 [45] J. Linnera and A. J. Karttunen, “Ab initio study of the lattice thermal conductivity
601 of Cu₂O using the generalized gradient approximation and hybrid density functional
602 methods,” *Physical Review B*, vol. 96, p. 014304, jul 2017.
- 603 [46] J. H. Skone, M. Govoni, and G. Galli, “Self-consistent hybrid functional for con-
604 densed systems,” *Physical Review B*, vol. 89, p. 195112, may 2014.
- 605 [47] A. Erba, “Self-consistent hybrid functionals for solids: a fully-automated implemen-
606 tation,” *Journal of Physics: Condensed Matter*, vol. 29, p. 314001, aug 2017.
- 607 [48] A. Živković, N. H. de Leeuw, B. G. Searle, and L. Bernasconi, “Electronic Excitations
608 in Copper Oxides: Time-Dependent Density Functional Theory Calculations with
609 a Self-Consistent Hybrid Kernel,” *The Journal of Physical Chemistry C*, vol. 124,
610 pp. 24995–25003, nov 2020.
- 611 [49] D. Broberg, B. Medasani, N. E. Zimmermann, G. Yu, A. Canning, M. Haranczyk,
612 M. Asta, and G. Hautier, “PyCDT: A Python toolkit for modeling point defects
613 in semiconductors and insulators,” *Computer Physics Communications*, vol. 226,
614 pp. 165–179, 2018.

- 615 [50] C. G. Van De Walle and J. Neugebauer, “First-principles calculations for defects and
616 impurities: Applications to III-nitrides,” *Journal of Applied Physics*, vol. 95, no. 8,
617 pp. 3851–3879, 2004.
- 618 [51] S. B. Zhang and J. E. Northrup, “Chemical potential dependence of defect formation
619 energies in GaAs: Application to Ga self-diffusion,” *Physical Review Letters*, vol. 67,
620 no. 17, pp. 2339–2342, 1991.
- 621 [52] C. Freysoldt, J. Neugebauer, and C. G. Van de Walle, “Fully Ab Initio Finite-Size
622 Corrections for Charged-Defect Supercell Calculations,” *Physical Review Letters*,
623 vol. 102, p. 016402, jan 2009.
- 624 [53] X. Rocquefelte, M.-H. Whangbo, A. Villesuzanne, S. Jobic, F. Tran, K. Schwarz,
625 and P. Blaha, “Short-range magnetic order and temperature-dependent properties
626 of cupric oxide,” *Journal of Physics: Condensed Matter*, vol. 22, p. 045502, feb 2010.
- 627 [54] X. Rocquefelte, K. Schwarz, and P. Blaha, “Theoretical Investigation of the Mag-
628 netic Exchange Interactions in Copper(II) Oxides under Chemical and Physical Pres-
629 sures,” *Scientific Reports*, vol. 2, p. 759, dec 2012.
- 630 [55] Z. Jiang, S. Tian, S. Lai, R. D. McAuliffe, S. P. Rogers, M. Shim, and D. P. Shoe-
631 maker, “Capturing Phase Evolution during Solvothermal Synthesis of Metastable
632 Cu_4O_3 ,” *Chemistry of Materials*, vol. 28, no. 9, pp. 3080–3089, 2016.
- 633 [56] J. Thanuja, Udayabhanu, G. Nagaraju, and H. R. Naika, “Biosynthesis of Cu_4O_3
634 nanoparticles using Razma seeds: application to antibacterial and cytotoxicity ac-
635 tivities,” *SN Applied Sciences*, vol. 1, p. 1646, dec 2019.
- 636 [57] A. Srikaow and S. M. Smith, “Preparation of $\text{Cu}_2(\text{OH})_3\text{NO}_3/\text{ZnO}$, a novel cata-
637 lyst for methyl orange oxidation under ambient conditions,” *Applied Catalysis B:*
638 *Environmental*, vol. 130-131, pp. 84–92, feb 2013.
- 639 [58] J. Medina-Valtierra, C. Frausto-Reyes, G. Camarillo-Martínez, and J. A. Ramírez-
640 Ortiz, “Complete oxidation of isopropanol over Cu_4O_3 (paramelaconite) coating de-
641 posited on fiberglass by CVD,” *Applied Catalysis A: General*, vol. 356, pp. 36–42,
642 mar 2009.
- 643 [59] D. R. Lide, *CRC Handbook of Chemistry and Physics, Internet Version 2005*. CRC
644 Press, Boca Raton, Fl, 2005.
- 645 [60] K. J. Blobaum, D. Van Heerden, A. J. Wagner, D. H. Fairbrother, and T. P. Weihs,
646 “Sputter-deposition and characterization of paramelaconite,” *Journal of Materials*
647 *Research*, vol. 18, pp. 1535–1542, jul 2003.

648 [61] C. L. Bailey, L. Liborio, G. Mallia, S. Tomić, and N. M. Harrison, “Defect physics
649 of CuGaS₂,” *Physical Review B*, vol. 81, p. 205214, may 2010.